Chemical Science

ROYAL SOCIETY OF CHEMISTRY

EDGE ARTICLE

View Article Online
View Journal | View Issue

Cite this: *Chem. Sci.*, 2025, **16**, 16915

All publication charges for this article have been paid for by the Royal Society of Chemistry

Stable and highly sensitive self-powered X-ray detection *via* high-density CsPbBr-type Dion–Jacobson trilayer hybrid perovskites

Huawei Yang,[a] Hang Li,[b] Jianbo Wu,[c] Zeng-Kui Zhu,*[a] Guirong Chen,[a] Guanghui Li,[a] Panpan Yu,[a] Ying Zeng,[a] Yueying Wang,[a] Wenhui Wu[a] and Junhua Luo *[ab]

Received 15th May 2025
Accepted 14th August 2025

DOI: 10.1039/d5sc03524d

rsc.li/chemical-science

Dion–Jacobson (DJ)-type organic–inorganic hybrid perovskites have emerged as promising candidates for X-ray detection owing to their exceptional stability and remarkable X-ray absorption ability. Nevertheless, achieving enhanced detection sensitivity continues to pose a significant challenge in this research domain. Herein, we have successfully synthesized and grown a DJ-type (4-AMP)$Cs_2Pb_3Br_{10}$ (**1**, 4-AMP^{2+} = 4-ammoniomethylpiperidinium) hybrid perovskite single crystal with a high density of 3.966 g cm^{-3}. This density value is the highest reported value in DJ-type hybrid perovskite materials to date. Benefiting from its high density that provides strong X-ray absorption capability, **1** exhibits excellent X-ray detection performance under a bias voltage of 100 V, achieving a sensitivity value of 6.1 × 10^3 μC Gy^{-1} cm^{-2}. This represents the highest value reported to date among CsPbBr-based DJ-type hybrid perovskites. Notably, **1** crystallizes in the polar space group $Pmc2_1$ and demonstrates remarkable self-powered X-ray detection capabilities, including a high sensitivity of 221.3 μC Gy^{-1} cm^{-2} and a low detection limit of 54.4 nGy s^{-1}. Excitingly, **1** also exhibits favourable environmental stability: after three months of ambient air exposure, the device retains 84.3% of its initial detection efficiency. This study provides valuable insights for advancing the development of high-performance X-ray detection devices with enhanced operational stability.

Introduction

Organic–inorganic hybrid perovskites (OIHPs) have shown great potential for development in the field of direct X-ray detection due to their strong X-ray absorption ability, large mobility–lifetime ($\mu\tau$) product, and cost-effective manufacturing process.[1–6] Notably, two-dimensional (2D) OIHPs have received widespread attention for their ability to effectively suppress ion migration and enhance material stability.[7–9] Recently, numerous high-performance X-ray detection materials based on the 2D Ruddlesden–Popper (RP) structure have been successfully developed, including $(BA)_2PbI_4$ (BA = *n*-butylamine),[10] $(F\text{-}PEA)_2PbI_4$ (F-PEA = 4-fluorophenylethylamine),[11] and $(o\text{-}F\text{-}PEA)_2PbI_4$ (*o*-F-PEA = 2-fluorophenethylam).[12] However, in the RP-type hybrid perovskite structure, the organic amine ligands between the layers are connected indirectly by relatively weak van der Waals interactions between two ions, resulting in weaker overall stability.[13] Furthermore, most of these detectors can only perform X-ray detection under external bias, which can cause severe ion migration and exacerbate their instability. Consequently, self-powered X-ray detection materials that can operate efficiently and stably without external voltage have attracted attention.[13–17] So far, several self-powered OIHP X-ray detectors such as $(3MeOPA)_2CsPb_2Br_7$ (3MeOPA = 3-methoxypropylamine),[18] IPA_2PbBr_4 (IPA = isopropyl ammonium),[19] and $(S\text{-}BPEA)_2FAPb_2I_7$ (BPEA = 1-4-bromophenylethylammonium)[20] have been reported successively. Although these RP-type devices have achieved great success in the field of X-ray detection, their inherent structural characteristics still necessitate further improvements in stability.

Dion–Jacobson (DJ)-type OIHPs have emerged as particularly promising materials in the field of X-ray detection, owing to their intrinsic properties, including enhanced stability and reduced interlayer spacing.[21–23] Compared to RP-type hybrid perovskites, the interlayer diamine ligands in DJ-type hybrid perovskites are directly connected to the inorganic framework through robust hydrogen bonding interactions. This not only shortens the interlayer spacing and improves carrier transport efficiency but also significantly enhances the rigidity and stability of the structure.[24–26] More importantly, the shorter spacing may induce the formation of halogen–halogen

[a]*College of Chemistry and Materials, Key Laboratory of Fluorine and Silicon for Energy Materials and Chemistry of Ministry of Education, Jiangxi Province Key Laboratory of Porous Functional Materials, Jiangxi Normal University, Nanchang, Jiangxi, 330022, China. E-mail: zkzhu@jxnu.edu.cn; jhluo@fjirsm.ac.cn*

[b]*State Key Laboratory of Functional Crystals and Devices, Fujian Institute of Research on the Structure of Matter, Chinese Academy of Sciences, Fuzhou, Fujian 350002, China. E-mail: jhluo@fjirsm.ac.cn*

[c]*Department of Materials Science and Engineering, City University of Hong Kong, Kowloon, Hong Kong SAR 999077, China*

interlayer coupling between adjacent inorganic layers to block the carrier recombination process, thus enabling the device to exhibit higher detection performance.[27,28] For instance, the DJ-type hybrid perovskite (3-MNPA)$PbBr_4$ (3-MNPA = 3-methylaminopropylamine)[29] exhibits excellent stability. After being placed in an air environment for one month, its light response and dark current remained largely unchanged. Similarly, the detection efficiency of the (4ABA)PbI_4 (4ABA = 4-aminobenzylamine)[30] device still retained 87.5% of its initial value after being placed in an air environment for 30 days. While these materials demonstrate excellent stability, there is still a need to enhance their sensitivity (3-MNPA)$PbBr_4$: 123 μC Gy^{-1} cm^{-2}; (4ABA)PbI_4: 572 μC Gy^{-1} cm^{-2}. Generally, materials with a high average atomic number and density tend to exhibit greater X-ray absorption efficiency, thereby enhancing the sensitivity.[31–34] Typically, a suitable strategy to increase the density involves incorporating small cations such as cesium (Cs^+), methylamine (MA^+), and ethylamine (EA^+) into 2D monolayers to construct multilayer hybrid perovskite materials. For example, the density of BA_2PbBr_4 is 2.44 g cm^{-3},[35] but when small cations are incorporated to form multilayer materials, the densities increase significantly. Specifically, the densities of $BA_2MAPb_2Br_7$, $BA_2MA_2Pb_3Br_{10}$, $BA_2CsPb_2Br_7$, and $BA_2Cs_2Pb_3Br_{10}$ increase to 2.87 g cm^{-3}, 3.05 g cm^{-3}, 3.11 g cm^{-3}, and 3.62 g cm^{-3}, respectively.[36–38] In particular, with the entry of heavy metal Cs^+ ions, the density of the material significantly increases. For instance, the three-layer structure containing two Cs^+ ions ($BA_2Cs_2Pb_3Br_{10}$) is much larger than the three-layer structure containing two MA^+ ions ($BA_2MA_2Pb_3Br_{10}$). Nevertheless, most of the DJ-type materials currently developed and used in the field of X-ray detection are single-layer, and high-density multilayer OIHPs are extremely rare. Only the three-layer hybrid perovskite (BDA)$(MA)_2Pb_3Br_{10}$ (BDA = 1,4-butanediamine)[39] based on MA^+ and the double-layer hybrid perovskite (BDA)$CsPb_2Br_7$,[40] containing Cs^+ have been reported. These materials achieve sensitivities of 1984 μC Gy^{-1} cm^{-2} and 725.5 μC Gy^{-1} cm^{-2}, respectively. Therefore, the development of high-density DJ-type multilayer hybrid perovskite X-ray detection materials capable of accommodating a large number of Cs^+ ions is of great significance for promoting the development of hybrid perovskite X-ray detectors.

In this work, we successfully synthesized and grew high-quality DJ-type three-layer high-density OIHP (4-AMP)$Cs_2Pb_3Br_{10}$ (**1**, 4-AMP^{2+} = 4-ammoniomethylpiperidinium). Crystal **1** exhibits an ultra-high density of 3.966 g cm^{-3}, which represents the highest reported density of both DJ-type and RP-type OIHPs to date. We studied semiconductor characteristics and X-ray detection performance based on single crystal **1**. Notably, **1** presents a large $\mu\tau$ value of up to 2.07×10^{-3} cm^2 V^{-1}. Under a bias voltage of 100 V, the sensitivity of **1** is as high as 6.1×10^3 μC Gy^{-1} cm^{-2}, which is currently the highest value reported for 2D CsPbBr-based DJ-type hybrid perovskites. Furthermore, **1** also demonstrates excellent self-powered detection performance, with a high sensitivity of 221.3 μC Gy^{-1} cm^{-2} and a low limit of detection (LoD) of 54.4 nGy s^{-1} even under zero bias voltage. Excitingly, **1** exhibits excellent stability, with a dark current drift of only 2.7×10^{-7} nA cm^{-1} s^{-1} V^{-1} at 100 V. Furthermore, it can operate continuously and stably under X-ray irradiation at a dose of 1.71 Gy. Even after being exposed to air for 3 months, it can still retain 84.3% and 85.2% of the initial state detection efficiency in self-powered mode and under 100 V bias, respectively. Our work confirms that DJ-type multi-layer high-density OIHPs are extremely promising materials for direct X-ray detection.

Results and discussion

The high-quality bulk single crystals of compound **1** (CCDC number: 2062501)[41] were successfully synthesized *via* the cooling growth method in a saturated hydriodic acid solution (Fig. S1; please refer to the synthesis and crystal growth section in the SI for details). Meanwhile, the phase purity of the crystals has been confirmed by powder X-ray diffraction (PXRD) analysis (SI, Fig. S2). The structural analysis shows that **1** has a typical two-dimensional DJ-type hybrid perovskite structure and crystallizes in the polar space group $Pmc2_1$. As shown in Fig. 1a, the inorganic layer consisting of the $PbBr_6$ octahedron is isolated by 4-AMP^{2+} organic cations, whereas the heavier Cs^+ ions are confined within the cavities of the $PbBr_6$ octahedron, resulting in a two-dimensional triple-layer structure. Specifically, as shown in Fig. 1b, the 4-AMP cations are interspersed and neatly arranged between the inorganic skeleton by strong bilateral N–H–Br hydrogen bonding forces and are tightly bound to the skeleton. Concurrently, the strong hydrogen bonding forces generated in this diamine cation drive both ends to be embedded in the skeleton to depths of 0.46 Å and 0.37 Å, respectively, ultimately resulting in a layer spacing of only 4.4 Å for **1** (Fig. 1a). This value is smaller than all DJ-type and RP-type CsPbBr-based hybrid perovskites except for (BDA)$CsPb_2Br_7$ (3.789 Å) (Fig. 1c).[18,38,40,42–52] Furthermore, we verified the interlayer spacing using the (2 0 0) peak of **1** in the XRD spectra of bulk single crystals,[53,54] and the results are highly compatible with the theoretical values (see Fig. S3 for details). Such a short interlayer spacing enables the organic diamine components between the layers to form strong hydrogen bonding forces with the inorganic skeleton. This strong hydrogen bonding interaction force increases lattice stiffness and suppresses electron–phonon coupling. Meanwhile, the separation and transport efficiency of charge carriers is improved, ultimately enabling high-performance X-ray detection.[23–26] To quantitatively assess the strength of these hydrogen bonding interactions, we conducted a Hirshfeld surface analysis. As shown in the fingerprint plots of Fig. S4, the total area of hydrogen bonds reached 44.6%, which confirms the existence of strong interactions in the structure. As shown in Table S1, the strength of hydrogen bonding forces in the structure was further verified by calculating bond lengths and bond angles. Overall, this strong interaction force not only facilitates the transport of charge carriers but also effectively stabilizes the structure.[55] To further investigate the electronic structure and semiconductor properties of the crystals, the energy band structure of material **1** was then calculated using density functional theory (DFT). As shown in Fig. S5a, the maximum value of the valence band (VBM) and the minimum value of the conduction band (CBM) are both

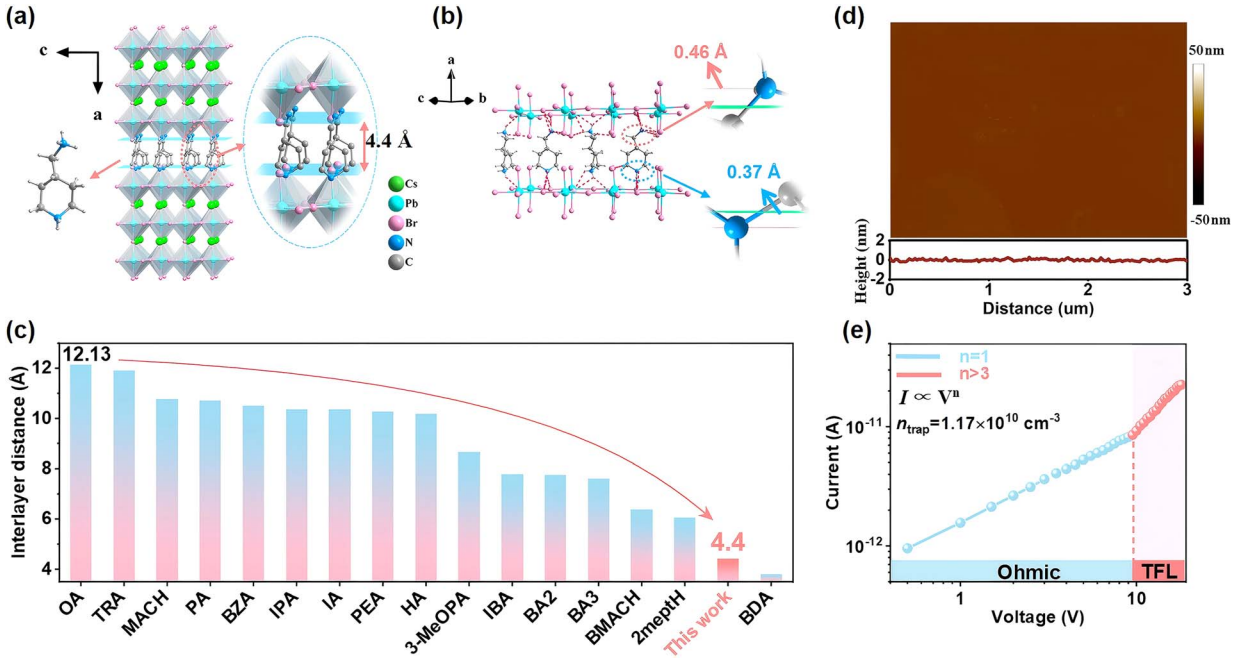

Fig. 1 (a) The crystal structure of **1** observed along the *c*-axis (the hydrogen atom was omitted for clarity of expression). (b) The interlayer hydrogen bonding forces and penetration depth of organic components (c) comparison of interlayer spacing between **1** and other CsPbBr-type OIHPs. OA, TRA, MACH, PA, BZA, IPA, IA, PEA, HA, 3-MeOPA, IBA, BA2, BA3, BMACH, 2meptH, and BDA respectively refer to $(OA)_2CsPb_2Br_7$ (OA = octylamine),[42] $(TRA)_2CsPb_2Br_7$ (TRA=(carboxy)cyclohexylmethylammonium),[43] $(MACH)_2CsPb_2Br_7$ (MACH = cyclohexylamine),[44] $(PA)_2CsPb_2Br_7$ (PA = *n*-pentylammonium),[45] $(BZA)_2CsPb_2Br_7$ (BZA = benzylamine),[46] $(IPA)_2CsPb_2Br_7$ (IPA = isopentylammonium),[47] $(IA)_2Cs3Pb_4Br_{13}$ (IA = isoamylammonium),[48] $(PEA)_2CsPb_2Br_7$ (phenylethylamine),[49] $(HA)_2CsPb_2Br_7$ (*n*-hexylammonium),[50] $(3\text{-MeOPA})_2CsPb_2Br_7$,[18] $(IBA)_2CsPb_2Br_7$ (IBA = isobutylamine),[51] $(BA)_2CsPb_2Br_7$,[38] $(BA)_2Cs_2Pb_3Br_{10}$,[38] (BMACH)$CsPb_2Br_7$ (BMACH = 1,3-cyclohexanedimethanaminium),[44] $(2meptH_2)CsPb_2Br_7$ (2-methyl-1,5-diaminopentane)[52] and (BDA)$CsPb_2Br_7$.[40] (d) The AFM image of the crystal **1** surface. (e) Logarithmic *I*–*V* of crystal **1** measured by the SCLC method.

located at point G1, indicating that it is a direct bandgap semiconductor with a bandgap value of 2.45 eV, which is in agreement with the value (2.36 eV) calculated by the Tauc method.[41] The partial density of states (PDOS) shows that there is a clear overlap between Pb 6s/6p and Br 4s/4p in the neighborhood of the Fermi level (Fig. S5b). This suggests that the octahedral inorganic skeleton of Pb/Br makes a significant contribution to the energy band gap.[45,46]

High-quality large crystals are a prerequisite for constructing X-ray detectors. Therefore, the surface of crystal **1** was evaluated by atomic force microscopy (AFM) and scanning electron microscopy (SEM). As illustrated in Fig. 1d and S6, the results showed that its surface was smooth and had no obvious defects. Furthermore, the measurement results of the trap state density (n_{trap}) of **1** using the space charge-limiting current (SCLC) method corroborate this conclusion (as illustrated in Fig. 1e, the actual electrode photo of device **1** during testing is shown in Fig. S7). The two regions in the current–voltage (*I*–*V*) curve, where the growth is relatively gentle and sharply increasing, are the ohmic region ($n = 1$) and the trap-filling (TFL) region ($n > 3$). The voltage at the inflection point is the trap-filled limited voltage (V_{TFL}), and the calculation formula is as follows:[56]

$$n_{trap} = \frac{2\varepsilon\varepsilon_0 V_{TFL}}{eL^2}$$

where the L, e, ε and ε_0 represent the interelectrode distance, the electron charge, the relative dielectric constant, and the absolute dielectric constant, respectively. The calculated n_{trap} of **1** is 1.17 $\times 10^{10}$ cm^{-3}, and such a low value is at least one order of magnitude lower than traditional inorganic semiconductors such as single-crystal silicon (Si) and CdTe/CdS thin-film (10^{13}–10^{14} cm^{-3} and 10^{11}–10^{13} cm^{-3}, respectively, at room temperature).[54,55] As shown in Table S2, the n_{trap} value of single-crystal **1** was compared with some reported perovskite single crystals and thin-film materials. The results indicate that the n_{trap} value of single crystal **1** is low, meaning that it has fewer defects. Furthermore, we tested SCLC on crystals with different thicknesses. As shown in Fig. S8, when the crystal thicknesses are 0.78 mm, 1.01 mm, and 1.36 mm, the n_{trap} values are 2.38 $\times$ 10^{10} cm^{-3}, 1.47 $\times$ 10^{10} cm^{-3}, and 3.66 $\times$ 10^{10} cm^{-3}, respectively. This result indicates that the crystal thicknesses have negligible influence on the n_{trap}, at least for our crystals. As shown in Fig. S9, the low defect state and long average charge carrier lifetime of **1** were analyzed through photoluminescence (PL) and time-resolved PL (see the SI for details). Such crystals with low defects and long carrier lifetimes are more conducive to realizing X-ray detection with high sensitivity and low detection limits. Besides, the thermal decomposition temperature curve shows that **1** only begins to decompose when the temperature reaches 610 K, which already exceeded most reported OIHPs, strongly confirming its excellent thermal stability

(Fig. S10 and Table S3). Given its unique structural characteristics, high crystal quality, and long carrier lifetime, crystal **1** demonstrates tremendous potential for efficient and stable X-ray detection applications.

The presence of a high average atomic number (Z) and heavy elements such as Cs, Pb, Br, *etc*. is beneficial for the effective absorption of high-energy X-rays.[30–33] The structural analysis results indicate that the density of **1** is as high as 3.966 g cm^{-3}. To our knowledge, this is the highest value in all DJ-type and RP-type CsPbBr-based hybrid perovskites (Fig. 2a).[16,37,39,41–51] The ability of materials to absorb X-ray photons is an important basis for the preliminary assessment of their potential for efficient direct X-ray detection. Therefore, we calculated the X-ray absorption of crystal **1** across a wide range of photon energies using a photon cross-section database. Within the wide range shown in Fig. 2b, the absorption coefficient of crystal **1** is superior to that of crystalline Si, CdTe, α-Se, $(BA)_2CsPb_2Br_7$, and $(BA)_2Cs_2Pb_3Br_{10}$.[37,54,55] Meanwhile, the attenuation efficiency of 50 keV X-ray photons is also significantly better than that of CdTe, α-Se, $(BA)_2CsPb_2Br_7$, and $(BA)_2Cs_2Pb_3Br_{10}$ (Fig. 2c). In addition, the $\mu\tau$ product is an important parameter for direct X-ray detectors, as it determines the charge collection efficiency of the X-ray detection materials. To evaluate the charge collection capability of **1**, we constructed a photoconductivity X-ray detector. As shown in Fig. 2d, the $\mu\tau$ product was derived by fitting the photoconductivity curve using a modified Hecht equation:[57]

$$I = \frac{I_0 u\tau V}{d^2}\left[1 - \exp\left(-\frac{d^2}{u\tau V}\right)\right]$$

where the I_0, V and d represent the saturated photocurrent, applied voltage, and distance between positive and negative electrodes. The fitted $\mu\tau$ product of **1** is 2.07 × 10^{-3} cm^2 V^{-1} at a dose rate of 1989 μGy s^{-1}. This value is equivalent to the classical 3D $MAPbI_3$ and much higher than commercial α-Se thin films (≈10^{-7} cm^2 V^{-1})[16] and other OIHP X-ray detectors, such as $(BDA)CsPb_2Br_7$ (2.33 ± 0.08) × 10^{-5} cm^2 V^{-1},[40] $(FPEA)_2PbI_4$ (5.1 × 10^{-4} cm^2 V^{-1}),[11] and $(BA)_2PbI_4$ (4.5 × 10^{-4} cm^2 V^{-1}).[10] The bulk photovoltaic effect (BPVE) is a unique phenomenon in polar materials that arises from the breaking of symmetry in crystalline materials. This phenomenon occurs readily in homogeneous materials with asymmetric centers. It manifests itself in the form of a material that produces a noticeable light voltage under uniform lighting conditions.[15,16] Considering that **1** is a polar material, there is a significant BPVE, which can spontaneously generate a photovoltage for X-ray detection.[18] So, the photovoltage of **1** was measured under a wavelength of 405 nm laser light source and different X-ray irradiation doses. As shown in Fig. S11 and 2e, the photovoltage values measured under 405 nm light sources and X-ray irradiation were 0.56 V and 0.53 V, respectively. Therefore, such a significant photovoltage can serve as a self-powered force to achieve X-ray detection without external bias. High resistivity (ρ) can effectively suppress dark current noise, making it more

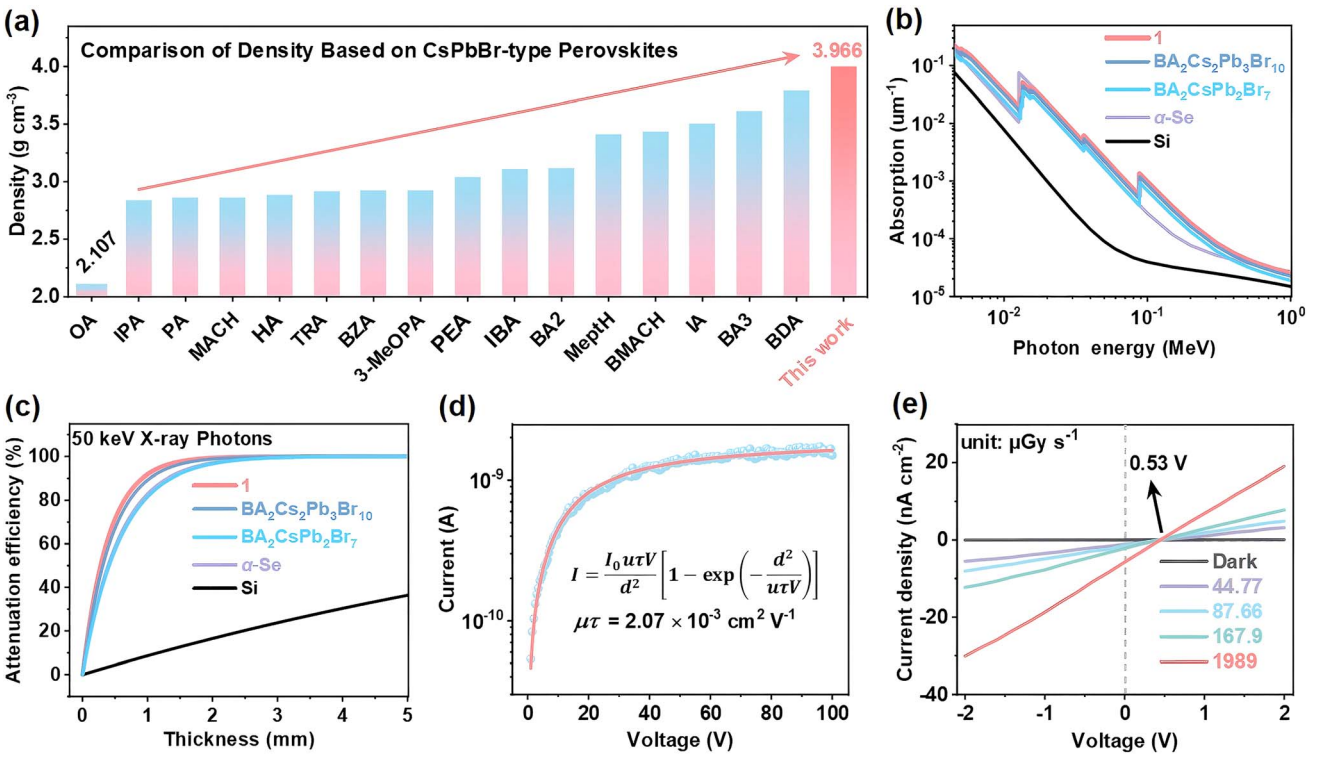

Fig. 2 (a) Comparison of the density of **1** with other reported CsPbBr-type perovskites. (b) X-ray photon absorption coefficient spectra of crystal **1**, Si, α-Se, $BA_2CsPb_2Br_7$ and $BA_2Cs_2Pb_3Br_{10}$. (c) Thickness-dependent attenuation efficiency of 50 keV X-ray photons on **1**, Si, α-Se, $BA_2CsPb_2Br_7$, and $BA_2Cs_2Pb_3Br_{10}$. (d) The voltage-dependent photoconductivity of **1** under X-ray irradiation along the c-axis. (e) The photovoltage of the crystal **1** detector under different X-ray irradiation conditions.

sensitive to X-rays. As shown in Fig. S12, the resistivity of device **1** measured to be as high as 4.55×10^{11} Ω cm, which was much higher than many reported OIHPs, such as (BDA)$CsPb_2Pb_7$ (4.35×10^{10} Ω cm),[40] (*S*-BPEA)$_2FAPb_2I_7$ (1.05×10^{10} Ω cm)[20] and the classic 3D OIHPs $Cs_2AgBiBr_6$ (1.6×10^{11} Ω cm) and $MAPbX_3$ (X = Cl, Br, I, 10^7–10^8 Ω cm).[58–60] This high resistivity not only indicates the high quality of crystal **1**, but also shows that it can effectively suppress dark current noise, thereby reducing the LoD.

Leveraging these significant advantages, we designed an X-ray detection device based on crystal **1** and rigorously evaluated its performance. As shown in Fig. 3a, the self-powered detection response in the absence of an applied bias was initially evaluated. With increasing X-ray doses from 1.09 μGy s^{-1} to 13.38 μGy s^{-1}, the response exhibited excellent linearity, accompanied by a significant increase in the response signal. The X-ray response of **1** was further evaluated under applied bias voltages of 10 V, 30 V, 50 V, 80 V, and 100 V (Fig. S13–S17). With the continuous increase in bias voltage, the response of the device also shows a significant increasing trend. This is attributed to the fact that device **1** has an increased charge collection efficiency in the presence of a high external electric field. Furthermore, the sensitivity of the X-ray response, a key parameter in measuring the detection performance of the device, is defined as follows:[61]

$$S = (J_p - J_d)/D$$

in the above equation, J_p and J_d represent the current densities observed under X-ray irradiation and in the absence of irradiation, respectively, and D denotes the X-ray dose rate. Fig. 3b shows that the response current density ($J_p - J_d$) of device **1** under X-ray irradiation exhibits a pronounced linear correlation with the sensitivity of device **1**. As shown in Fig. 3c, after applying a bias voltage from 10 V to 100 V, the charge collection efficiency of the device also improved, significantly enhancing the sensitivity of device **1**. At a bias voltage of 100 V, its sensitivity achieved an impressive 6103.5 μC Gy^{-1} cm^{-2}, greater than some reported similar materials such as (BDA)$MA_4Pb_5I_{16}$ (4853 μC Gy^{-1} cm^{-2}),[23] (BDA)$CsPb_2Br_7$ (725.5 μC Gy^{-1} cm^{-2}),[40] and (4ABA)PbI_4 (572 μC Gy^{-1} cm^{-2}).[30] In fact, this value represents the highest reported value of DJ-type OIHP based on CsPbBr and the highest record among all known DJ-type hybrid perovskites except for (3AMPY)$(FA)Pb_2I_7$,[62] (5.23×10^4 μC Gy^{-1} cm^{-2} under 200 V bias, 3AMPY = 3-aminomethylpyridine) to date (Table S4). Meanwhile, the sensitivity of the device in self-powered mode was 221.3 μC Gy^{-1} cm^{-2}, which is an exciting value. Due to the correlation between the electrode spacing L of the detector and the sensitivity value, we have supplemented the X-ray detection performance of different electrode spacings in self-powered mode. As shown in Fig. S18, the detection sensitivity of the device gradually decreases with the increase of electrode spacing L, which is consistent with some previously reported literature studies.[63] As illustrated in Tables S4 and S5, these values are higher than those of the majority of traditional

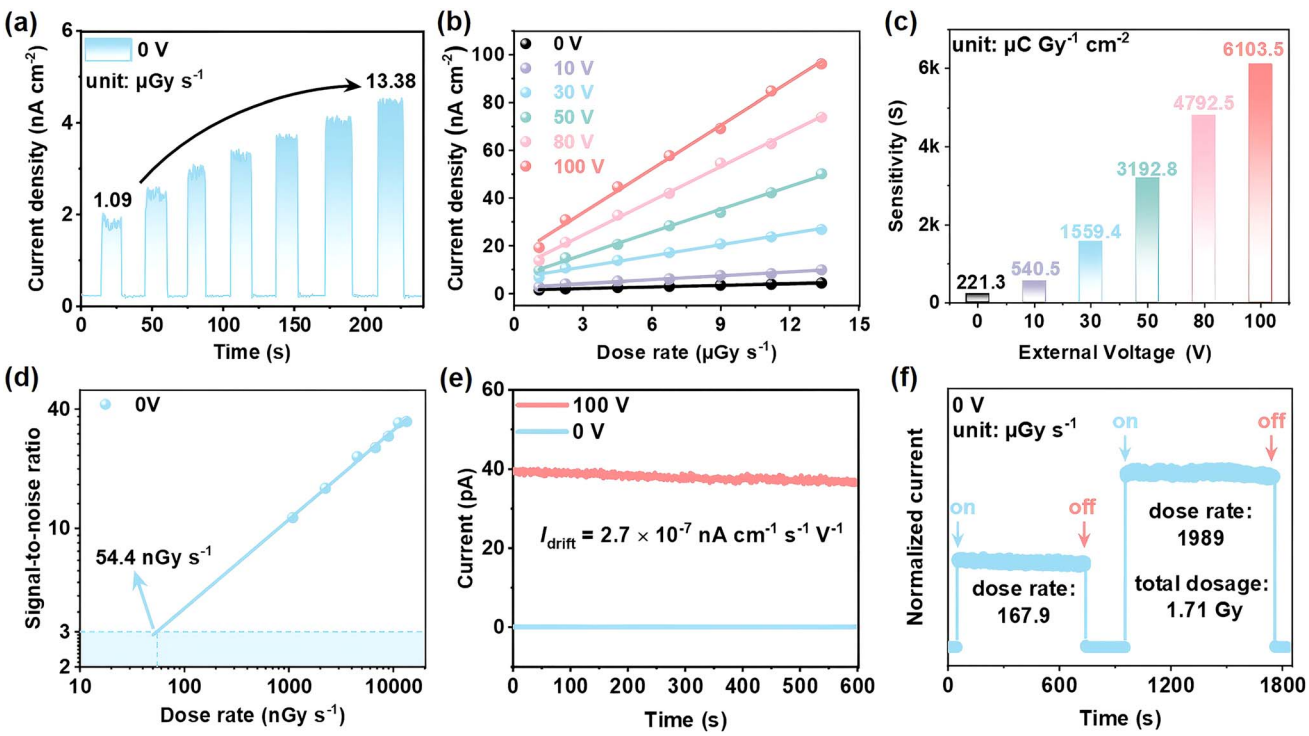

Fig. 3 (a) The current density–time curve of device **1** under 0 V bias as the X-ray radiation dose increases. (b and c) Fitting to obtain the X-ray detection sensitivity of device **1** under different bias voltages. (d) The signal-to-noise ratio (SNR) of device **1** under 0 V bias. (e) Dark current drift of device **1** under 0 V and 100 V bias voltage, respectively. (f) Response stability of device **1** under different high X-ray dose rate irradiation conditions for a long time.

inorganic materials and many reported X-ray detectors, including α-Se thin-film (20 μC Gy^{-1} cm^{-2} under 2000 V bias),[64] Si single crystals (8 μC Gy^{-1} cm^{-2} under 0.5 V bias),[65] $(S\text{-BPEA})_2FAPbI_7$ (87.8 μC Gy^{-1} cm^{-2} under 0 V bias),[20] and $(BA)_2PbI_4$ (148 μC Gy^{-1} cm^{-2} under 10 V mm^{-1} bias).[10] The LoD is another crucial parameter for assessing X-ray detection performance. In accordance with the definition of the International Union of Pure and Applied Chemistry (IUPAC), the X-ray dose rate at a signal-to-noise ratio (SNR) of 3 is used as the detection limit of the X-ray detector.[66] According to the following equation, the SNR value can be measured:

$$\mathrm{SNR} = \frac{\overline{I_{\mathrm{ph}}} - \overline{I_{\mathrm{d}}}}{\sqrt{\frac{1}{N}\sum_{i}^{n}\left(I_i - \overline{I_{\mathrm{ph}}}\right)^2}}$$

where $\bar{I}_{\mathrm{ph}}$ denotes the average photocurrent, $\bar{I}_{\mathrm{d}}$ denotes the average dark current, and I_i denotes the measured photocurrent. In self-powered mode, the LoD calculation of device **1** is as low as 54.4 nGy s^{-1} (Fig. 3d). This value is comparable to some advanced detectors such as $(iBA)_2CsPb_2Br_7$ (72.5 nGy s^{-1})[51] and $(BDA)MA_4Pb_5I_{16}$ (39 nGy s^{-1}),[23] and is about 100 times lower than that of traditional medical detection materials (α-Se, 5500 nGy s^{-1}).[67] Such a low value of LoD has great potential in reducing the damage of X-ray radiation to the human body. In addition, we also calculated the LoD of device **1** under different bias voltages (Fig. S19–S23). The results indicate that device **1** still has a low detection limit of 619.2 nGy s^{-1} at a high external bias voltage of 100 V. The severity of ion-migration under X-ray irradiation is another important parameter for evaluating the performance of X-ray detectors, which can be demonstrated by the magnitude of dark current drift (I_{drift}). It can be obtained from the following equation:[68]

$$I_{\mathrm{drift}} = \frac{(I_t - I_0)}{E \times A \times t}$$

where I_0 and I_t are the initial and final currents, E is the electric field, and A is the device area, respectively. Notably, even under a high bias voltage of 100 V, the I_{drift} value of device **1** is only 2.7 × 10^{-7} nA cm^{-1} s^{-1} V^{-1}, let alone at 0 V bias (Fig. 3e). This further confirms the device's extremely low ion migration and stable dark current in self-powered mode. Additionally, the ability of device **1** to maintain sustained and stable operation under long-term X-ray irradiation is also crucial in practical applications. To evaluate this, we exposed device **1** to two high X-ray doses of 167.9 μGy s^{-1} and 1989 μGy s^{-1} and operated it continuously for over 1200 seconds (Fig. 3f). Impressively, after receiving a high dose of radiation of 1.71 Gy continuously, the X-ray response intensity and dark current magnitude remained highly stable. Moreover, we further tested the X-ray on/off cycle stability of the device in self-powered mode at two different X-

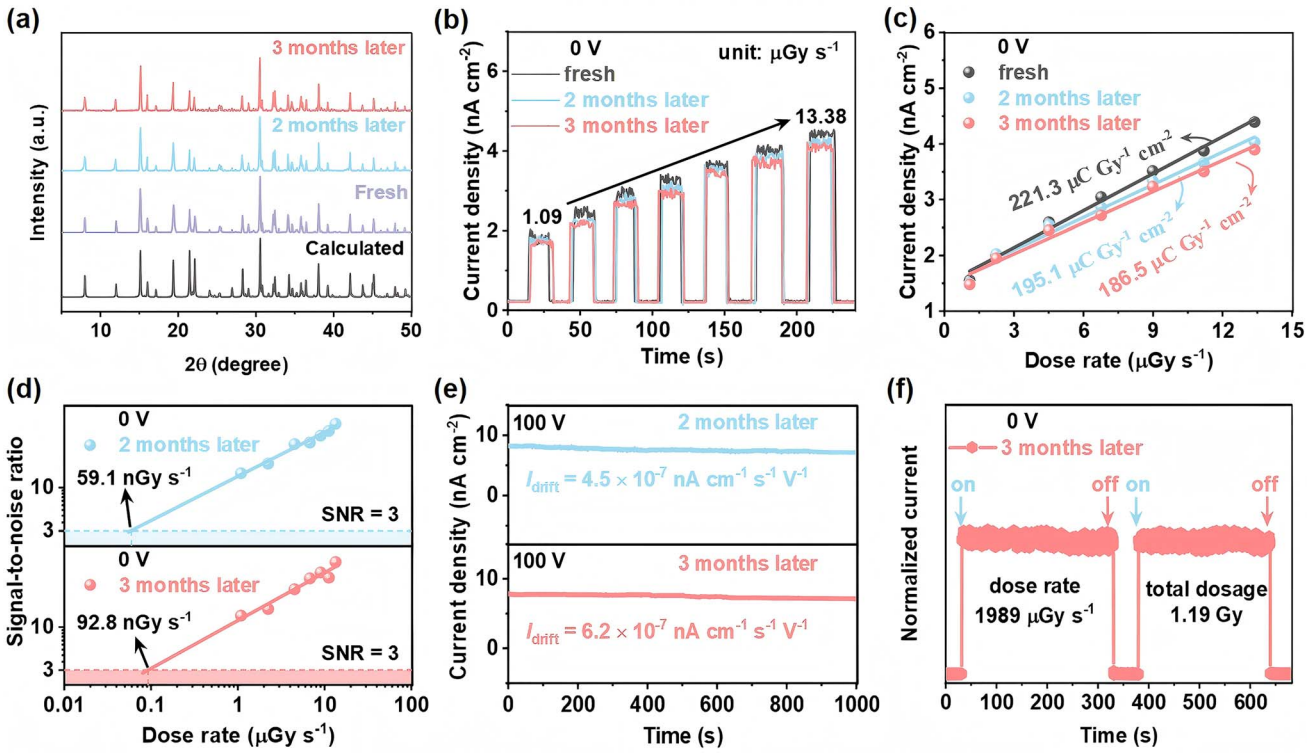

Fig. 4 (a) Comparison of the purity of the powder after being placed in an air environment for 2 and 3 months, respectively. (b) The current density–time curve of device **1** after 2 and 3 months of exposure to dry air. (c) Comparison of sensitivity and initial sensitivity of device **1** under 0 V bias after 2 and 3 months of exposure to air. (d) Comparison of the SNR of device **1** with the initial value after 2 and 3 months under 0 V bias. (e) The dark current drift values of device **1** after being placed in air for 2 and 3 months, respectively. (f) Stability of device **1** under long-term high-dose rate X-ray irradiation after being exposed to air for 3 months.

ray doses of 167.9 μGy s^{-1} and 1989 μGy s^{-1}. As shown in Fig. S24, after 40 cycles of continuous operation under these two X-ray doses, the response current of device **1** remained almost unchanged. These demonstrate that device **1** is capable of long-term continuous operation without performance degradation.

The ability of device **1** to maintain stability in an air environment is a significant factor in evaluating its performance and potential for commercial development. Next, we verified the environmental stability of device **1**. As shown in Fig. 4a, the purity of the powder was tested after exposure to air for two and three months. The results showed that there was no significant change in the PXRD pattern of **1**, confirming its excellent phase stability. Then, the X-ray response capability of device **1** was tested after two months and three months (Fig. 4b). It can be seen that the response signal of device **1** hardly changed significantly after two and three months. In Fig. 4c, the sensitivities of the device were calculated to be 195.1 μC Gy^{-1} cm^{-2} and 186.5 μC Gy^{-1} cm^{-2} after two and three months, respectively. These values maintained 88.2% and 84.3% of their initial efficiency, respectively. The X-ray response of the device under 100 V bias after three months in the air environment was also evaluated (Fig. S25). As anticipated, the device continues to exhibit a high sensitivity of 5200.5 μC Gy^{-1} cm^{-2}, thereby preserving an initial efficiency of 85.2% (Fig. S26). More importantly, device **1** still retains an extremely low LoD of 59.1 nGy s^{-1} and 92.8 nGy s^{-1} after two and three months, respectively (Fig. 4d). And three months later, the LoD at 100 V bias was only 770.2 nGy s^{-1} (Fig. S27). In addition, under the 100 V bias voltage, the dark current drift of the device was measured to be 4.5×10^{-7} nA cm^{-1} s^{-1} V^{-1} and 6.2×10^{-7} nA cm^{-1} s^{-1} V^{-1} after two months and three months, respectively, thereby demonstrating its excellent stability (Fig. 4e). Finally, the anti-fatigue ability of the device was tested after three months. As shown in Fig. 4f, the device can still maintain a highly stable operation after receiving a total dose of 1.19 Gy of X-ray radiation. These results confirm the excellent environmental stability of the device. Therefore, our work fully proves that the OIHP material with ultra-high density and multiple layers is a quite advanced self-powered X-ray detection material.

Conclusions

In summary, we successfully synthesized and grew high-quality DJ-type three-layer OIHP (4-AMP)$Cs_2Pb_3Br_{10}$ crystals. It is worth noting that due to the large amount of heavy metal Cs^+ in crystal **1**, the density is as high as 3.966 g cm^{-3}, which is the highest value in DJ-type OIHPs. In addition, the AMP^{2+} diamine cation in **1** reduces the interlayer spacing to 4.4 Å, which enables it to transport carriers more efficiently. Based on the excellent characteristics of **1** mentioned above, we investigated its semiconductive properties and X-ray detection performance. **1** exhibits a large $\mu\tau$ of 2.07×10^{-3} cm^2 V^{-1} and achieves a sensitivity of 6.1×10^3 μC Gy^{-1} cm^{-2} under 100 V bias, which is currently the highest value reported for 2D CsPbBr-based DJ-type hybrid perovskites. Furthermore, in self-powered mode, device **1** has a high sensitivity of 221.3 μC Gy^{-1} cm^{-2} and an ultra-low LoD of 54.4 nGy s^{-1}. More importantly, the X-ray detection efficiency of device **1** remained 88.2% and 84.3% of the initial efficiency even after continuous exposure to air for 2 and 3 months, respectively, demonstrating its favourable stability. Our work confirms that DJ-type multi-layer high-density OIHPs represent an extremely promising material for X-ray detection and provide a new path for the development of efficient X-ray detectors.

Author contributions

H. W. Yang synthesized the bulk single crystal, measured the related properties including X-ray detection performances, and wrote this manuscript. H. Li and J. B. Wu measured thermal decomposition curves, AFM, and SEM plots. G. R. Chen, G. H. Li, and P. P. Yu analysed and discussed the experimental data. Y. Zeng, Y. Y. Wang, and W. H. Wu provided some suggestions for the project. J. H. Luo and Z.-K. Zhu designed and directed this project. All authors discussed and commented on the manuscript.

Conflicts of interest

The authors declare that they have no conflict of interest.

Data availability

The data supporting the findings of this study are available within the SI. See DOI: **https://doi.org/10.1039/d5sc03524d**.

Acknowledgements

This work was financially supported by the National Natural Science Foundation of China (22435005, 22193042, 22201284, 21921001, 22305105, 22405108, 22125110, 22122507, and U21A2069), the Natural Science Foundation of Fujian Province (2023J05076), the Natural Science Foundation of Jiangxi Province (20252BAC200222, 20242BAB25129, 20224BAB213003, and 20232BAB213020), and the Jiangxi Provincial Education Department Science and Technology Research Foundation (GJJ2200384).

References

1 H. Wei and J. Huang, *Nat. Commun.*, 2019, **10**, 1066.
2 Y. Li, Y. Lei, H. Wang and Z. Jin, *Nano-Micro Lett.*, 2023, **15**, 128.
3 X. He, M. Xia, H. Wu, X. Du, Z. Song, S. Zhao, X. Chen, G. Niu and J. Tang, *Adv. Funct. Mater.*, 2021, **32**, 2109458.
4 Y. Shen, Y. Liu, H. Ye, Y. Zheng, Q. Wei, Y. Xia, Y. Chen, K. Zhao, W. Huang and S. F. Liu, *Angew. Chem., Int. Ed.*, 2020, **59**, 14896.
5 Z. Li, Y. Sun, Y. Zhang, J. Zhao and H. Zhao, *J. Ind. Eng. Chem.*, 2024, **134**, 592–599.
6 Z. Li, Y. Sun, F. Han, Y. Wang, J. Li, N. Zhang, B. Tian and H. Zhao, *ChemistrySelect*, 2023, **8**, e202301851.
7 L. Gao, J. You and S. F. Liu, *J. Energy Chem.*, 2021, **57**, 69–82.

8 B. Xiao, Q. Sun, F. Wang, S. Wang, B.-B. Zhang, J. Wang, W. Jie, P. Sellin and Y. Xu, *J. Mater. Chem. A*, 2021, **9**, 13209–13219.
9 Z.-K. Zhu, T. Zhu, S. You, P. Yu, J. Wu, Y. Zeng, Q. Guan, Z. Li, C. Qu, H. Zhong, L. Li and J. Luo, *Small*, 2024, **20**, 2307454.
10 J. G. Yukta, M. A. Afroz, S. Alghamdi, P. J. Sellin and S. Satapathi, *ACS Photonics*, 2022, **9**, 3529–3539.
11 H. Li, J. Song, W. Pan, D. Xu, W.-a. Zhu, H. Wei and B. Yang, *Adv. Mater.*, 2020, **32**, 2003790.
12 B. Zhang, Z. Xu, C. Ma, H. Li, Y. Liu, L. Gao, J. Zhang, J. You and S. F. Liu, *Adv. Funct. Mater.*, 2022, **32**, 2110392.
13 Q. Fan, H. Xu, S. You, Y. Ma, Y. Liu, W. Guo, X. Hu, B. Wang, C. Gao, W. Liu, J. Luo and Z. Sun, *Small*, 2023, **19**, 2301594.
14 S. You, Z. K. Zhu, S. Dai, J. Wu, Q. Guan, T. Zhu, P. Yu, C. Chen, Q. Chen and J. Luo, *Adv. Funct. Mater.*, 2023, **33**, 2303523.
15 J. Wu, S. You, P. Yu, Q. Guan, Z.-K. Zhu, Z. Li, C. Qu, H. Zhong, L. Li and J. Luo, *ACS Energy Lett.*, 2023, **8**, 2809–2816.
16 Z.-K. Zhu, T. Zhu, J. Wu, S. You, P. Yu, X. Liu, L. Li, C. Ji and J. Luo, *Adv. Funct. Mater.*, 2023, 2214660.
17 Y. Ma, W. Li, Y. Liu, W. Guo, H. Xu, S. Han, L. Tang, Q. Fan, J. Luo and Z. Sun, *ACS Cent. Sci.*, 2023, **9**, 2350–2357.
18 Y. Dang and X. Tao, *Matter*, 2022, **5**, 2659–2684.
19 Y. He, Z. Chen, D.-W. Fu, Z. Hou, X.-M. Zhang and D. Fu, *Chem. Mater.*, 2024, **36**, 994–1003.
20 Q. Guan, H. Ye, S. You, Z.-K. Zhu, H. Li, X. Liu and J. Luo, *Small*, 2024, **20**, 2307908.
21 G. Chen, H. Dai, Z.-K. Zhu, J. Wu, P. Yu, Y. Zeng, Y. Zheng, L. Xu and J. Luo, *Small*, 2024, **20**, 2312281.
22 W. Guo, H. Xu, Q. Fan, P. Zhu, Y. Ma, Y. Liu, X. Zeng, J. Luo and Z. Sun, *Adv. Opt. Mater.*, 2024, **12**, 2303291.
23 L. Tao, L. Ding, Y. Li, H. Liu, M. Gao, D. Yang and Y. Fang, *J. Mater. Chem. C*, 2024, **12**, 18757–18764.
24 W. Guo, Z. Yang, J. Dang and M. Wang, *Nano Energy*, 2021, **86**, 106129.
25 B. Zhang, T. Zheng, J. You, C. Ma, Y. Liu, L. Zhang, J. Xi, G. Dong, M. Liu and S. F. Liu, *Adv. Mater.*, 2023, **35**, 2208875.
26 A. J. L. Johnston, S. Hoogland, E. H. Sargent and D. S. Seferos, *J. Am. Chem. Soc.*, 2021, **143**, 19901–19908.
27 W. Ke, L. Mao, C. Stoumpos, J. Hoffman, I. Spanopoulos, A. Mohite and M. Kanatzidis, *Adv. Energy Mater.*, 2019, **9**, 1803384.
28 X. Li, W. Ke, B. Traore, P. Guo, I. Hadar, M. Kepenekian, J. Even, C. Katan, C. Stoumpos, R. Schaller and M. Kanatzidis, *J. Am. Chem. Soc.*, 2019, **141**, 12880–12890.
29 Y. Fan, Q. Chen, Z. Li, T. Zhu, J. Wu, S. You, S. Zhang, J. Luo and C. Ji, *Small*, 2023, **19**, 2303814.
30 Q. Fan, Y. Ma, S. You, H. Xu, W. Guo, Y. Liu, L. Tang, W. Li, J. Luo and Z. Sun, *Adv. Funct. Mater.*, 2024, **34**, 2312395.
31 R. Zhuang, X. Wang, W. Ma, Y. Wu, X. Chen, L. Tang, H. Zhu, J. Liu, L. Wu, W. Zhou, X. Liu and Y. Yang, *Nat. Photonics*, 2019, **13**, 602.
32 C. Wu, Q. Zhang, G. Liu, Z. Zhang, D. Wang, B. Qu, Z. Chen and L. Xiao, *Adv. Energy Mater.*, 2020, **10**, 1902496.
33 C.-F. Wang, H. Li, M. G. Li, Y. Cui, X. Song, Q.-W. Wang, J.-Y. Jiang, M.-M. Hua, Q. Xu, K. Zhao, H.-Y. Ye and Y. Zhang, *Adv. Funct. Mater.*, 2021, **31**, 2009457.
34 C.-F. Wang, H. Li, Q. Ji, C. Ma, L. Liu, H.-Y. Ye, B. Cao, G. Yuan, H.-F. Lu, D.-W. Fu, M.-G. Ju, J. Wang, K. Zhao and Y. Zhang, *Adv. Funct. Mater.*, 2022, **32**, 2205918.
35 L. Dou, A. B. Wong, Y. Yu, M. Lai, N. Kornienko, S. W. Eaton, A. Fu, C. G. Bischak, J. Ma, T. Ding, N. S. Ginsberg, L.-W. Wang, A. P. Alivisatos and P. Yang, *Science*, 2015, **349**, 1518–1521.
36 L. Li, X. Liu, Y. Li, Z. Xu, Z. Wu, S. Han, K. Tao, M. Hong, J. Luo and Z. Sun, *J. Am. Chem. Soc.*, 2019, **141**, 2623–2629.
37 L. Li, Z. Sun, P. Wang, W. Hu, S. Wang, C. Ji, M. Hong and J. Luo, *Angew. Chem., Int. Ed.*, 2017, **56**, 12150.
38 H. Chen, J. Lin, J. Kang, Q. Kong, D. Lu, J. Kang, M. Lai, L.-N. Quan, Z. Lin, J. Jin, L.-w. Wang, M. F. Toney and P. Yang, *Sci. Adv.*, 2020, **6**, eaay4045.
39 S. Wang, F. Wang, X. Xu, N. Zhang, R. Zhang, L. Lv, X. Jiang, X. Huang, S. Wu and Y. Ding, *ACS Appl. Mater. Interfaces*, 2023, **15**, 58566–58572.
40 B. Xiao, Q. Sun, S. Wang, L. Ji, Y. Li, S. Xi, B.-B. Zhang, J. Wang, W. Jie and Y. Xu, *J. Phys. Chem. Lett.*, 2022, **13**, 1187–1193.
41 Z. Wang, X. Zhang, H. Ye, T. Zhu and J. Luo, *Chem.–Eur. J.*, 2022, **28**, e202200849.
42 Y. Liu, M. Siron, D. Lu, J. Yang, R. Reis, F. Cui, M. Gao, M. Lai, J. Lin, Q. Kong, T. Lei, J. Kang, J. Jin, J. Ciston and P. Yang, *J. Am. Chem. Soc.*, 2019, **141**, 13028–13032.
43 Y. Liu, J. Wang, S. Han, X. Liu, M. Li, Z. Xu, W. Guo, M. Hong, J. Luo and Z. Sun, *Chem.–Eur. J.*, 2020, **26**, 3494.
44 Q.-Q. Jia, H.-F. Ni, M.-M. Lun, L.-Y. Xie, H.-F. Lu, D.-W. Fu and Q. Guo, *J. Mater. Chem. C*, 2022, **10**, 16330–16336.
45 W. Guo, H. Xu, Y. Ma, Y. Liu, H. Gao, T. Hu, W. Ren, J. Luo and Z. Sun, *Angew. Chem., Int. Ed.*, 2023, **62**, e202300028.
46 Y. Yao, Y. Peng, L. Li, X. Zhang, X. Liu, M. Hong and J. Luo, *Angew. Chem., Int. Ed.*, 2021, **60**, 10598.
47 M. Li, S. Han, Y. Liu, J. Luo, M. Hong and Z. Sun, *J. Am. Chem. Soc.*, 2020, **142**, 20744–20751.
48 W. Guo, H. Xu, Y. Ma, Y. Liu, B. Wang, L. Tang, L. Hua, J. Luo and Z. Sun, *Adv. Funct. Mater.*, 2022, **32**, 2207854.
49 L. N. Quan, Y. Park, P. Guo, M. Gao, J. Jin, J. Huang, J. K. Copper, A. Schwartzberg, R. Schaller, D. T. Limmer and P. Yang, *Proc. Natl. Acad. Sci. U. S. A.*, 2021, **118**, e2104425118.
50 Y. Liu, X. Pan, X. Liu, S. Han, J. Wang, L. Lu, H. Xu, Z. Sun and J. Luo, *Small*, 2022, **18**, 2106888.
51 Z. Wu, X. Liu, C. Ji, L. Li, S. Wang, Y. Peng, K. Tao, Z. Sun, M. Hong and J. Luo, *J. Am. Chem. Soc.*, 2019, **141**, 3812–3816.
52 D. Fu, S. Wu, J. Xin, X. Zhang, G. Han and X.-M. Zhang, *Chem. Commun.*, 2020, **56**, 14381–14384.
53 Y. Wang, D. Yan, L. Wang, D. Wang and B. Z. Tang, *Adv. Sci.*, 2021, **8**, 2100811.
54 C. Lee, H. Lee, C.-S. Jeong, S. Ma, G. Jang, Y. Park, J. Yun, J. Lee, J. Son, W. Jeong, S. Yang, J. Park, K. Woo and J. Moon, *ACS Energy Lett.*, 2024, **9**, 4032–4043.
55 A. Balcioglu, R. K. Ahrenkiel and F. Hasoon, *J. Appl. Phys.*, 2000, **88**, 7175.

56 J. Di, H. Li, J. Su, H. Yuan, Z. Lin, K. Zhao, J. Chang and Y. Hao, *Adv. Sci.*, 2022, **9**, 2103482.
57 Y. Wang, Q. Guan, Z.-K. Zhu, H. Ye, H. Li, Y. Zeng, P. Yu, H. Yang, W. Wu and J. Luo, *Chem. Sci.*, 2025, **16**, 5283–5288.
58 A. Balcioglu, R. K. Ahrenkiel and F. Hasoon, *J. Appl. Phys.*, 2000, **88**, 7175–7178.
59 Y. C. Kim, K. H. Kim, D. Y. Son, D. N. Jeong, J. Y. Seo, Y. S. Choi, I. T. Han, S. Y. Lee and N. G. Park, *Nature*, 2017, **550**, 87.
60 Z. Xu, X. Liu, Y. Li, X. Liu, T. Yang, C. Ji, S. Han, Y. Xu, J. Luo and Z. Sun, *Angew. Chem., Int. Ed.*, 2019, **58**, 15757.
61 M. Ge, S. Chen, X. Fu, Y. Feng, D. Wang and M. Yuan, *J. Phys. Chem. C*, 2022, **126**, 19417–19423.
62 D. Fu, Z. Hou, Y. He, H. Wu, S. Wu, Y. Zhang, G. Niu and X.-M. Zhang, *ACS Appl. Mater. Interfaces*, 2022, **14**, 11690–11698.
63 S. Gavranovic, J. Pospisil, O. Zmeskal, V. Novak, P. Vanysek, K. Castkova, J. Cihlar and M. Weiter, *ACS Appl. Mater. Interfaces*, 2022, **14**, 20159–20167.
64 Z. Xu, H. Wu, D. Li, W. Wu, L. Li and J. Luo, *J. Mater. Chem. C*, 2021, **9**, 13157–13161.
65 W. Pan, H. Wu, J. Luo, Z. Deng, C. Ge, C. Chen, X. Jiang, W.-J. Yin, G. Niu, L. Zhu, L. Yin, Y. Zhou, Q. Xie, X. Ke, M. Sui and J. Tang, *Nat. Photonics*, 2017, **11**, 726.
66 S. O. Kasap, *J. Phys. D: Appl. Phys.*, 2000, **33**, 2853.
67 G. Rikner and E. Grusell, *Phys. Med. Biol.*, 1983, **28**, 1261.
68 Z. Li, F. Zhou, H. Yao, Z. Ci, Z. Yang and Z. Jin, *Mater. Today*, 2021, **48**, 155–175.